FRiED: A NOVEL THREE-DIMENSIONAL MODEL OF CORONAL MASS EJECTIONS

A. Isavnin
Department of Physics, University of Helsinki, Helsinki, Finland; alexey.isavnin@helsinki.fi
Received 2016 September 2; revised 2016 November 4; accepted 2016 November 4; published 2016 December 21

ABSTRACT

We present a novel three-dimensional (3D) model of coronal mass ejections (CMEs) that unifies all key evolutionary aspects of CMEs and encapsulates their 3D magnetic field configuration. This fully analytic model is capable of reproducing the global geometrical shape of a CME with all major deformations taken into account, i.e., deflection, rotation, expansion, "pancaking," front flattening, and rotational skew. Encapsulation of 3D magnetic structure allows the model to reproduce in-situ measurements of magnetic field for trajectories of spacecraft-CME encounters of any degree of complexity. As such, the model can be used single-handedly for the consistent analysis of both remote and in-situ observations of CMEs at any heliocentric distance. We demonstrate the latter by successfully applying the model for the analysis of two CMEs.

Key words: methods: data analysis – Sun: coronal mass ejections (CMEs)

1. INTRODUCTION

Coronal mass ejections (CMEs) are large-scale explosive eruptions of magnetized plasma from the Sun into the heliosphere. In addition to being one of the most spectacular manifestations of solar activity, these phenomena are the strongest drivers of space weather and one of the major hazards for space exploration (Lanzerotti 2001). A useful space weather forecast in relation to a CME is expected to predict reliably both time and strength of its impact on space environment. Both of these characteristics strongly depend on global geometry and internal structure of CME and its evolution (Lee et al. 2014).

Our understanding of CMEs has largely improved over the last two decades due to increasingly detailed remote and in-situ observations of the Sun and advances in modeling and simulation techniques. High-resolution extreme ultraviolet observations have given insight to mechanisms of CME initiation and strong support for their underlying magnetic flux-rope structure (Vourlidas 2014). Flux-rope eruption is thus the most favorable mechanism of CME known to date (Chen 2011). Flux-rope formation prior to ejection was further confirmed by extreme ultraviolet observations of the solar disk (Patsourakos et al. 2013). Stereoscopic white-light coronagraph observations of solar eruptions have given rise to the three-dimensional (3D) geometrical modeling of CMEs (Thernisien et al. 2006, 2009) a.k.a. forward modeling (FM). The latter facilitated the studies of CME deflections and rotations (Gui et al. 2011; Vourlidas et al. 2011) and propagation dynamics (Poomvises et al. 2010) in the inner heliosphere. Heliospheric imaging has provided a way to study CME propagation all the way from Sun to Earth (Eyles et al. 2009). The emerged modeling techniques facilitated the development of propagation tools for the estimation of CME arrival times (Lugaz et al. 2009; Davies et al. 2013; Möstl & Davies 2013; Rollett et al. 2013). Various flux-rope fitting models and reconstruction techniques have been developed, which allow us to infer local properties of flux-rope CMEs using single- or multi-spacecraft in-situ measurements (Hidalgo et al. 2002b; Hu & Sonnerup 2002; Owens et al. 2006; Möstl et al. 2009b; Isavnin et al. 2011; Nieves-Chinchilla et al. 2016).

By combining remote-sensing and in-situ analysis techniques at different heliocentric distances, it has become possible to study evolution of CMEs during their propagation through interplanetary space (Yurchyshyn et al. 2009; Isavnin et al. 2013, 2014; Kay et al. 2013) and their internal configuration (Kilpua et al. 2013). However, the majority of current techniques and models consider only limited subsets of CME properties and often make inconsistent assumptions about its structure. Hence, attempts to combine different models to gain the full picture of a CME have limited effectiveness. Another promising approach to this challenge is empirical 3D modeling of CMEs. Given the large amount of in-situ observations of these structures, it has become possible to deduce the mean statistical configuration of CMEs outside the coronagraph field of view (Janvier et al. 2013) as well as of shock wave fronts associated with them (Démoulin et al. 2016). These studies show that such phenomena as CMEs have certain generic 3D morphology. Therefore, the complexity of each individual CME results from specific deformations that it experienced in the interplanetary medium.

Major evolutionary deformations that CMEs experience during propagation through interplanetary space can be classified into self-similar expansion, change of orientation (deflections and rotations), front flattening, kinematic distortion due to radial expansion, a.k.a., "pancaking," and rotational skewing due to the rotation of the Sun. Internal magnetic field structure of a CME also undergoes changes consequent to its deformations. The impact of a CME on space environment is directly related to its magnetic field configuration at a given location, which in turn depends on its global 3D geometrical and morphological structure.

In this work, we present a novel 3D model of CMEs that is capable of reproducing all of their major deformations. The model embeds also 3D magnetic field structure and is capable of describing both remote and in-situ observations of CMEs. We demonstrate the performance of the model with two case studies of CMEs.

2. MODEL

We start by defining a 3D shell of the CME and then we populate it with magnetic field. First, we consider a simplified representation of CME as a bunch of magnetic field lines attached by both ends to the Sun and forming a croissant-like shape (Figure 1(a)). Heliocentric distance to the apex (the
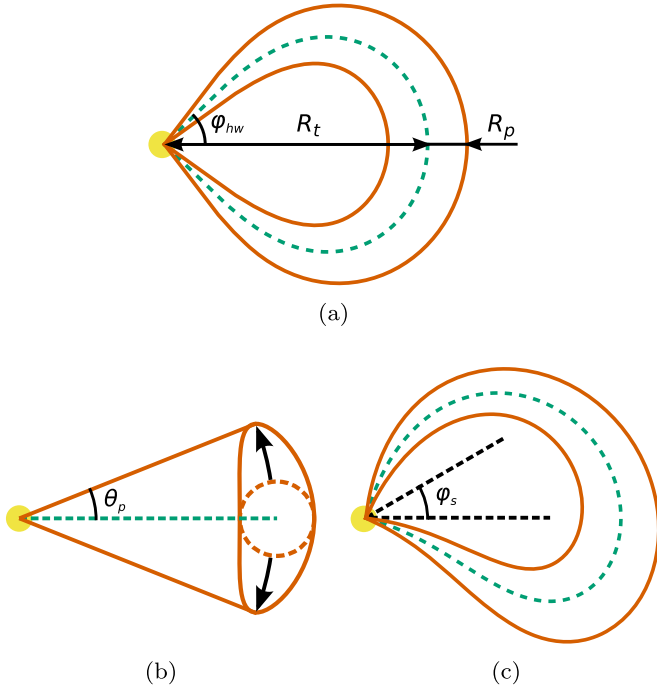
Figure 1. Schematic representation of a CME (a) and its pancaking (b) and skewing (c) deformations.

furthermost point) of the axis of the structure is its toroidal height R_t. We further assume that this quasi-CME has a circular cross-section anywhere perpendicular to its axis. The radius of the cross-section varies proportionally to the heliocentric distance with the largest in the apex of the structure (we call it poloidal height and denote it as R_p) and tending to zero in the Sun as

$$R(\varphi) = \frac{D(\varphi)}{2} = \frac{R_p}{R_t} r(\varphi), \tag{1}$$

where $R(\varphi)$ and $D(\varphi)$ are radius and diameter of the cross-section and $r(\varphi)$ describes the axis of the structure in polar coordinates.

This 3D structure is assumed to be in equilibrium in the stream of hydrodynamic wind radially outflowing from the Sun with constant speed. By equilibrium, we understand the balance between the forces of magnetic tension ($\boldsymbol{F}_B$), gravity ($\boldsymbol{F}_G$), and hydrodynamic streamlining ($\boldsymbol{F}_H$):

$$\boldsymbol{F}_H = \boldsymbol{F}_G + \boldsymbol{F}_B \tag{2}$$

For the sake of simplicity, we assume the equilibrium to be quasistatic, i.e., the structure is similar to a non-propagating slingshot in a radial outflow. In our simplified description, we assume the background solar wind to be purely hydrodynamic and non-magnetized. Equation (2) does not take into account magnetic pressure since there is no magnetic interaction between the structure and the background wind. For a small piece of the structure along its axis, the curvature of the axis and the variability of poloidal radius can be neglected thus making it reasonable to use cylindrical coordinates. The radial and azimuth projections of the balance Equation (2) for a small section of the structure along its axis can then be written as

$$dF_D = dF_G + dF_B \cos \alpha, \tag{3}$$

$$dF_L = dF_B \sin \alpha, \tag{4}$$

where dF_D and dF_L are the forces of hydrodynamic drag and lift that act in radial and azimuth directions, respectively, and $\alpha(\varphi)$ is the angle between normal to the axis and radial direction determined as

$$\cos^2 \alpha = \frac{r^2}{r^2 + r'^2} \tag{5}$$

Assuming that the shape of the structure can be locally described as a cylinder with diameter given by Equation (1), drag and lift forces can be estimated as

$$dF_D = \frac{1}{2}\rho v^2 C_D(\alpha) D(\varphi) ds, \tag{6}$$

$$dF_L = \frac{1}{2}\rho v^2 C_L(\alpha) D(\varphi) ds, \tag{7}$$

where ρ and v are the density and velocity of the radial outflow. C_D and C_L are the drag and lift coefficients that can be estimated for a cylinder (Vakil & Green 2009) as

$$C_D(\alpha) = \frac{C_D^0}{2}(1 + \cos 2\alpha), \tag{8}$$

$$C_L(\alpha) = C_L^0 \sin 2\alpha. \tag{9}$$

C_D^0 is the maximum of the drag coefficient of a cylinder, which happens when it is positioned perpendicularly to the flow. C_L^0 is the maximum of the lift coefficient, which happens when a cylinder is positioned at $\pi/4$ angle to the flow. Using Equations (7) and (9), we can rewrite Equation (4) as

$$\rho v^2 C_L^0 D(\varphi) \cos \alpha = \frac{B_0^2}{2\mu_0} \kappa(\varphi), \tag{10}$$

where $\kappa(\varphi)$ is the curvature of the axis of the structure defined in polar coordinates as

$$\kappa(\phi) = \frac{1}{R_c(\phi)} = \frac{r^2 + 2r'^2 - rr''}{(r^2 + r'^2)^{3/2}}, \tag{11}$$

where $R_c(\varphi)$ is the curvature radius. Putting together Equations (5), (10), and (11), we arrive to the following equation:

$$r^2(r^2 + 2r'^2 - rr'') = A(r^2 + r'^2), \tag{12}$$

where A combines all the constants of this simplified problem:

$$A = \frac{\rho v^2 C_L^0 R_p \mu_0}{B_0 R_t}. \tag{13}$$

The numerical solution, which describes the axis of the structure, is shown in Figure 2(a) along with the guessed approximate solution:

$$r(\varphi) = R_t \cos^n(a\varphi). \tag{14}$$

Here, $a = (\pi/2)/\varphi_{hw}$, where φ_{hw} is angular half-width of the axis of the structure. It can be seen from Figure 2(a) that the approximate solution (Equation (14)) to the balance equation describes the axis of the structure exceptionally well compared to the numerical one and thus sufficiently reproduces the physics of our simplified problem. Hence, we will utilize it in our model for simplicity of further calculations. Coefficient n
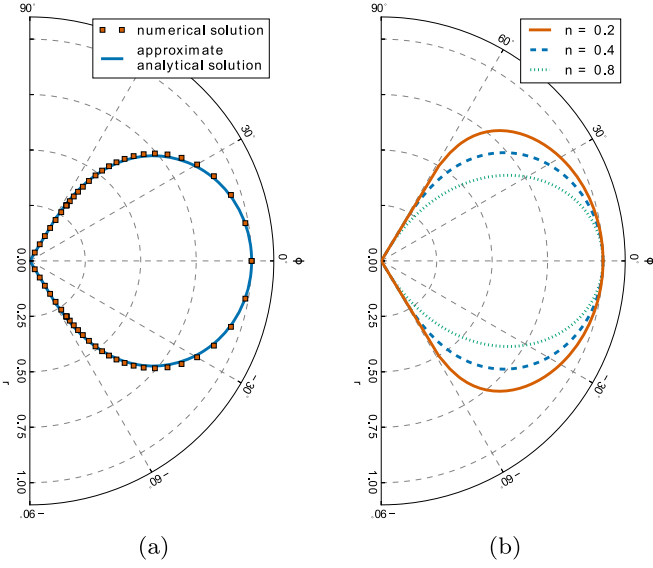
(a)   (b)

Figure 2. Numerical and approximate solutions to balance equation (a). Front flattening of the approximate solution (b). The half-width was kept constant at 60°.

(a)   (b)   (c)

Figure 3. Global deformation of 3D CME shell: front flattening (a), pancaking (b), and skewing (c).

regulates the front flattening of the structure (Figure 2(b)). Summarizing, the 3D geometry of our model CME at this stage represents a loop structure attached to the Sun by both ends with axis given by Equation (14) and circular cross-section diameter given by Equation (1).

Analytic representation of our 3D shell makes it straightforward to apply global deformations to it. Front flattening deformation happens to CMEs propagating much faster than the speed of the background solar wind (Vršnak et al. 2013). The speed difference causes the drag, which flattens the front of the CME and slows down its propagation. This type of deformation is naturally supported by the model through coefficient n (Figure 2(b)). Another type of global deformation often omitted in CME analysis is "pancaking" distortion. This deformation is a direct consequence of radial propagation of CME through interplanetary space and has a purely kinematic nature (Cargill 2004; Riley et al. 2004). We implement this effect in our shell model as a latitudinal stretch, which is characterized by pancaking angle θ_p (Figure 1(b)). This parameter describes vertical half-width of a CME and can be considered to be a natural counterpart to the lateral half-width φ_{hw}. If both half-width φ_{hw} and pancaking angle θ_p do not change during the propagation of a CME one can conclude that its angular size is conserved. Finally, we implement skew as a rotational deformation around the Z axis with the skewing angle of φ_s (Figure 1(c)). Skewing happens due to rotation of the Sun and is more pronounced for slow CMEs. In Figure 3, we demonstrate these three types of global deformations in 3D. Apparently, the global orientation of the 3D shell is also easily adjustable, which makes it capable of reproducing deflections and rotations.

At this point, our CME shell model is characterized by nine free parameters: toroidal height R_t, poloidal height R_p, angular half-width φ_{hw}, front flattening coefficient n, pancaking angle θ_p, skewing angle φ_s, direction of propagation (latitude θ and longitude φ), and tilt angle γ.

Now that we have a highly flexible 3D shell of a CME, we need to populate it with magnetic field. The inner morphology of a CME is typically described by magnetic flux-rope
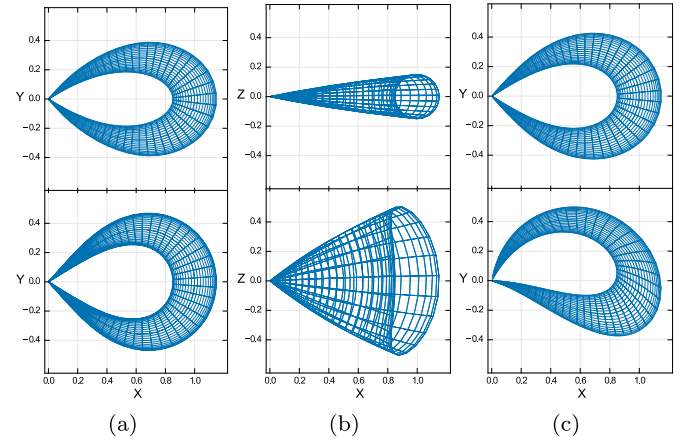
structure. Classical flux rope represents an idealized configuration of magnetic field characterized by the following properties: local cylindrical geometry, helical magnetic field lines with zero twist in the core and increasing to infinity close to the edge of a flux rope, and maximum magnetic field strength along the axis of the flux rope (Russell 1999). Such a configuration is often estimated with the Lundquist model, which describes cylindrical magnetic geometry in the force-free field (Lundquist 1950). However, recent studies of field line twist and length distributions within magnetic flux ropes in CMEs report inconsistencies with the Lundquist model. Hu et al. (2015) showed that in-situ measurements of interplanetary CMEs are consistent with a flux-rope structure with spiral field lines of constant and low twist. We use the latter finding for the construction of the 3D configuration of magnetic field lines for our model.

We start with a collection of parallel magnetic field lines contained in a cylinder of unit radius. The direction of the magnetic field is characterized by polarity equal to either $+1$ or -1, which corresponds to east–west or west–east directions of core magnetic field of a flux rope. The length of the cylinder is set to the length L of the axis of the CME shell:

$$L = \int_{-\varphi_{hw}}^{\varphi_{hw}} \left[r^2 + \left(\frac{dr}{d\varphi} \right)^2 \right]^{1/2} d\varphi. \qquad (15)$$

The strength of magnetic field is estimated using the distribution of magnetic field from the Lundquist model:

$$B(\rho) = B_0 \left[J_0^2(\alpha\rho) + J_1^2(\alpha\rho) \right]^{1/2}, \qquad (16)$$

where ρ is poloidal distance from the axis, B_0 is the strength of the core field, J_0 and J_1 are Bessel functions of the first and second order, and $\alpha\rho$ gives the first zero of J_0 at the edge of the flux rope. We then apply twisting deformation with constant twist τ, tapering deformation according to Equation (1) and bend the structure to the shape defined by Equation (14). The direction of the twist is characterized by chirality that can be equal to $+1$ or -1, which corresponds to right- or left-handedness of a flux rope respectively. Thereafter, pancaking and skewing deformations can be applied to the resultant magnetic field structure in the same way as we applied them to the shell earlier.

Lastly, we introduce conservation of magnetic flux Φ into our model:

$$\Phi = \iint_S \boldsymbol{B} \cdot \boldsymbol{ds}. \tag{17}$$

In the simplest case without pancaking and skewing deformations the cross-section of the structure perpendicular to its axis remains circular. Equation (17) can then be simplified to the following form:

$$\Phi = 2\pi \int_0^{\rho_0} B(\rho)\cos(\delta)\rho d\rho, \tag{18}$$

where

$$\delta = \arctan\frac{2\pi\rho\tau}{L}. \tag{19}$$

The flux conservation is introduced by varying axial field B_0 in Equation (16) along the axis of the structure so that integral Equation (18) remains constant, i.e., B_0 is weakest in the apex and strongest in the footpoints. After the introduction of pancaking and skewing deformations, the distribution given by Equation (16) distorts accordingly. In such a case in the current version of the model, we estimated magnetic flux given by Equation (17) numerically.

By adding magnetic structure to the model, we introduced two free parameters, i.e., twist τ and magnetic flux Φ, and two binary parameters, i.e., polarity and chirality. The final model of a flux rope in 3D (FRi3D) is shown in Figure 4. Due to flux conservation the model naturally supports magnetic field expansion. Figure 5 shows a narrow slice of magnetic field lines of the FRi3D model near its apex. The shape of the cross-section demonstrates pancaking deformation, while the distribution of magnetic field follows the deformation accordingly.

Simulation of in-situ measurements of evolving CMEs is made straightforward and natural with the FRi3D model. Figure 6 shows simple examples of such synthetic measurements of magnetic field given in the Heliocentric Earth Equatorial coordinate system (HEEQ, Thompson 2006). In these examples, it is assumed that a CME is propagating along the Sun–Earth line with zero tilt and is measured in-situ by a synthetic spacecraft located in the Lagrangian point 1 (L1). The model CME has the following parameters: $\theta = 0°$, $\varphi = 0°$, $\gamma = 0°$, $R_p = 0.15$ au, $n = 0.5$, $\varphi_{\mathrm{hw}} = 40°$, $\theta_p = 30°$, $\varphi_s = 0°$, $\tau = 3$, $\Phi = 5e14$ Wb, positive polarity and positive chirality. The top panel of Figure 6 shows synthetic spacecraft measurements of a non-evolving CME, i.e., a snapshot of a magnetic field profile. One could think of it as a measurement made by a spacecraft passing through a static CME with $R_t = 1$ au and not vice versa. The observed rotation of magnetic field is typical for a flux-rope CME. However, even in such a simplified scenario differences from cylindrical flux-rope models arise. For example, the asymmetry in the B_y component of the magnetic field is caused by two 3D geometrical factors: first, the bending of magnetic field into a CME shape distorts field lines slightly stronger on the front part of a CME than on a back one; and, second, pancaking deformation also distorts magnetic field lines stronger on the front part of a CME than on a back one. The middle panel of Figure 6 presents the case of the simplest evolution of a CME. The CME is set to propagate radially from the Sun by

increasing R_t, while all other parameters are kept constant:

$$R_t = R_{t0} + V_{R_t}t, \tag{20}$$

where V_{R_t} is the speed of propagation, i.e., the speed of toroidal height growth. Constancy of θ_p naturally introduces dynamic pancaking deformation, which gradually increases the area of the CME cross-section, while it propagates and thus causes magnetic expansion. That is why the most obvious difference from the previous example is the shift of the maximum of total magnetic field to the start of the measurement. The total duration of the measurement remained the same, since the CME did not experience any expansion in R_p. Finally, the bottom panel of Figure 6 shows the same example with added poloidal expansion introduced via increasing R_p:

$$R_p = R_{p0} + V_{R_p}t, \tag{21}$$

where V_{R_p} is the speed of poloidal height growth. In this case, the total duration of the measurement stretched due to increased radial size of the CME cross-section. The maximum of the total magnetic field shifted to the start of the measurement even more, because magnetic expansion happened at a higher rate.

3. CASE STUDIES

In this section, we present example case studies of two CMEs using the FRi3D model. Since we analyze remote and in-situ observations with the same model, we require both of these measurements to be clear and non-ambiguous. Both CMEs for our analysis were selected using HELiospheric Cataloguing And Techniques Service (HELCATS).

In our first case study, we present a CME that was released on 2010 December 12 at 02:48 UT as a prominence eruption from the southern hemisphere. This CME was observed in white-light by coronagraphs on board *SOHO* (Domingo et al. 1995) and *STEREO* (Kaiser et al. 2008) spacecraft (Figure 7). The erupting loop appeared as a partial halo in *STEREO-A* field of view and backside partial halo in *STEREO-B* field of view. The CME did not produce any visible signatures of a shock wave. According to *SOHO* observations, the erupting structure smoothly and quickly accelerated to a projected speed of 545 km s^{-1} and kept it steady during further propagation in the coronagraph field of view.

Lower panels of Figure 7 show the fit of the FRi3D model to coronagraph images from COR2 and C3 instruments on board *STEREO* and *SOHO* spacecraft respectively. The model performs in a similar way as Graduated Cone Shell model (GCS, Thernisien et al. 2009) successfully reproducing the the bright flux-rope loop of the CME. The parameters of the fit are summarized in Table 1.

Interplanetary counterpart of this CME reached *STEREO-A* spacecraft on 2010 December 15. The corresponding magnetic obstacle measured between 10:20 UT of December 15 and 04:00 UT of December 16 demonstrated smooth rotation of magnetic field, low proton temperature and proton density, as well as bi-directional electron flows (Figure 8), i.e., the typical signatures of a magnetic cloud (Zurbuchen & Richardson 2006).

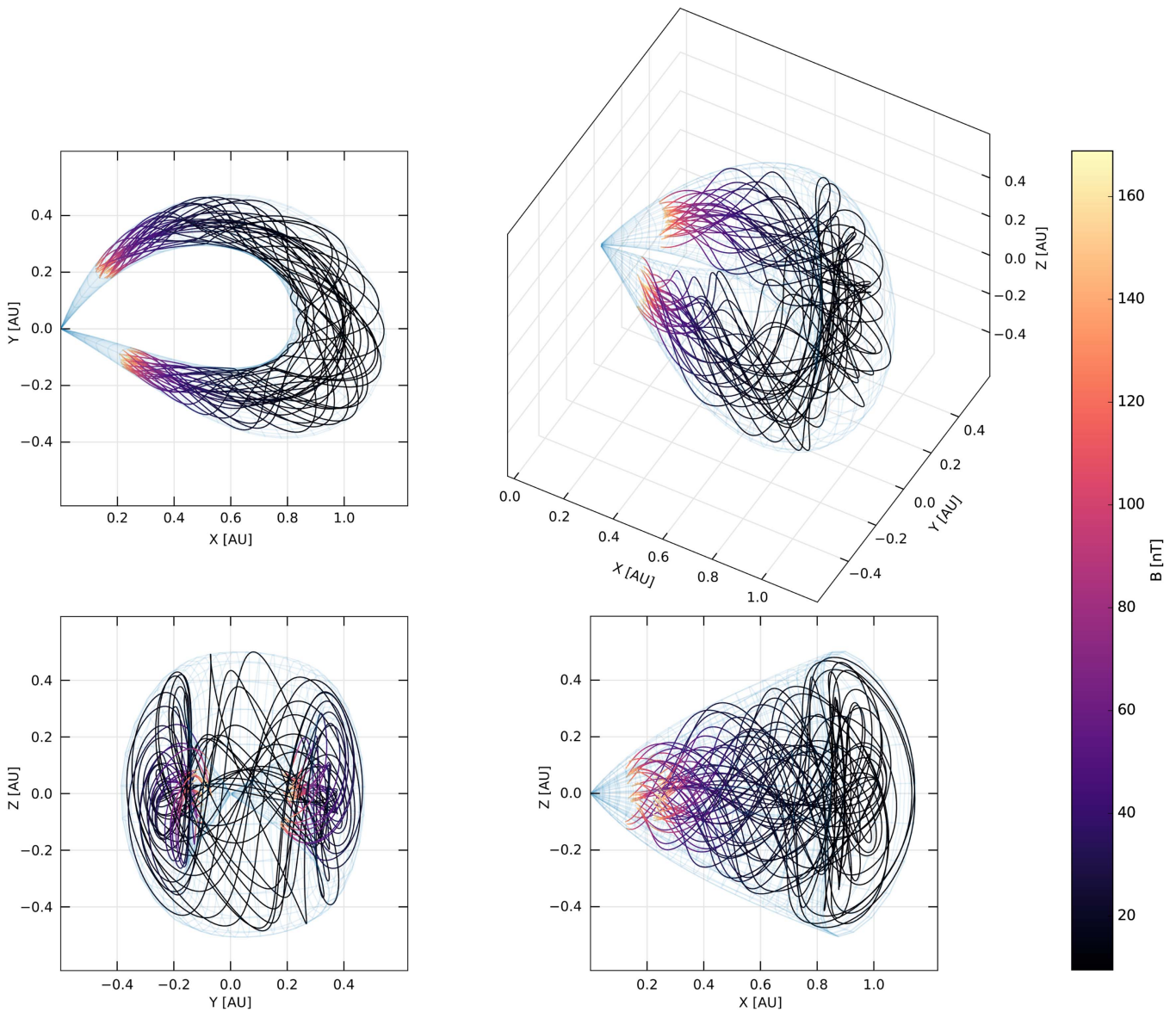For the sake of simplicity, when fitting the FRi3D model to in-situ data, we assume that

Figure 4. FRi3D model of a CME depicted in top, front, side, and isometric views. The shell of the model is shown with transparent blue wireframe. Each of 30 randomly selected lines represents an individual magnetic field line. The strength of magnetic field along each line is color-coded. Note that magnetic lines are not shown close to the Sun, because strong gradient of magnetic field would render color-coding useless.

1. the CME does not experience any evolution apart from pancaking deformation while passing the spacecraft, i.e., the case shown in the middle panel of Figure 6;
2. the speed of CME propagation V_{R_t} is constant and is equal to average speed of magnetic obstacle measured in-situ;
3. there are no constraints on the geometrical parameters of the CME resulting from our fit to remote data (Figure 7), i.e., we obtain all 3D geometrical parameters of the CME from in-situ data independently from remote observations.

The numerical fitting is carried using a differential evolution algorithm (Storn & Price 1997), which represents a real-valued version of genetic algorithm. Differential evolution does not use gradient methods to find the best fit and can search large areas of candidate parameter space. It does not rely on starting parameters either. The initial population of possible solutions is chosen randomly from the parameter space. At each pass through the population, the algorithm mutates each candidate

solution by mixing with other candidate solutions to create a trial candidate. The operation continues until a sufficiently fit candidate solution is obtained. The time range of magnetic obstacle is set to be soft, i.e., the fitting algorithm is allowed to go beyond the specified temporal boundaries by ± 2 hr. The quality of the fit is assessed by average euclidean distance between the real and synthetic measurements. The fitting procedure was run several times to ensure the uniqueness of its convergence. The best fit is shown in Figure 8, while the fitted parameters of the FRi3D model are listed in Table 1. The average euclidean distance between the modeled and real data is 2.85 nT.

Independent fits of the FRi3D model to remote and in-situ data show that the strongest geometrical changes were seen in latitude θ and tilt γ of the CME. According to modeling results it experienced latitudinal deflection and rotation and ended up lying almost perfectly in solar equatorial plane, which agrees with earlier findings by Isavnin et al. (2013, 2014). The
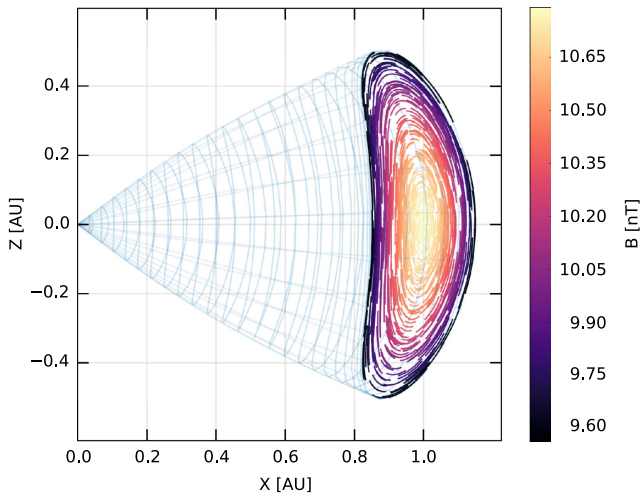
Figure 5. Cross-section of the FRi3D model near its apex. The colored lines are the sections of magnetic field lines near the apex. The strength of the magnetic field is color-coded.
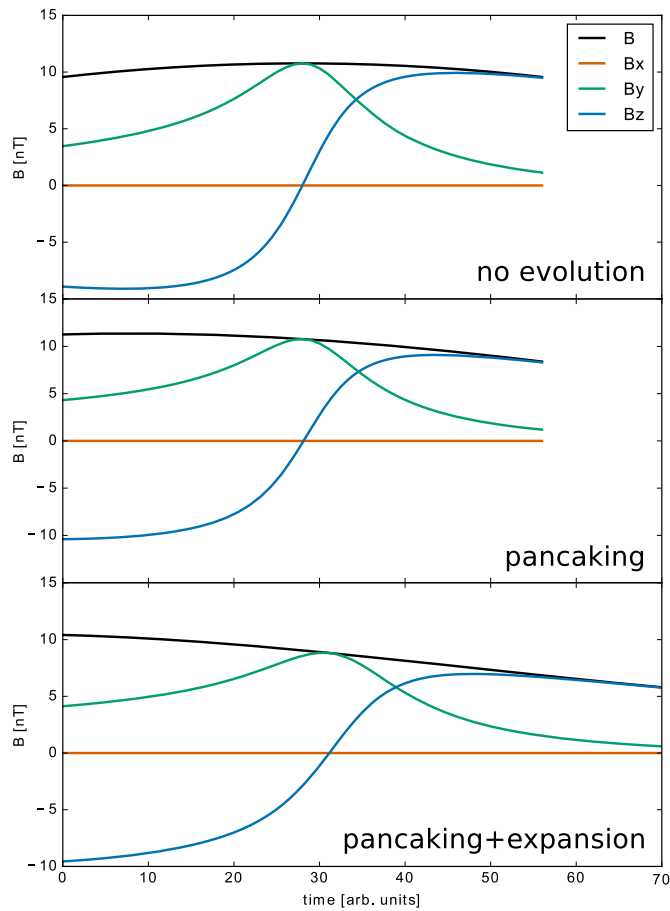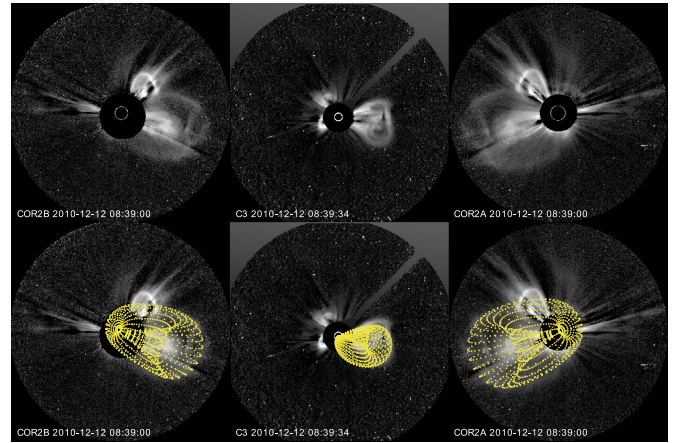

Figure 7. Coronagraph images of the CME released on 2010 December 12. The images from left to right show observations from COR2 coronagraph of *STEREO-B*, C3 coronagraph of *SOHO*, and COR2 coronagraph of *STEREO-B*, respectively. Lower panels show the fitting of the FRi3D model to coronagraph observations.

Table 1
Parameters of the FRi3D Model Fits to Remote and In-situ Data for CME Launched on 2010 December 12

	θ	φ	R_p/R_t	φ_{hw}	γ	n	θ_p
Remote	−14.5	55.0	0.28	55.0	16.0	0.60	23.0
in-situ	0.0	59.7	0.10	66.8	0.2	0.62	29.3
...			$\tau = 4.2$, $\Phi = 4.7 \times 10^{14}$ Wb				
...			west–east polarity, right-handed				

Figure 6. Examples of synthetic in-situ measurements of magnetic field using the FRi3D model. The top panel shows a magnetic field snapshot of a non-evolving CME, the middle panel portrays CME propagation with a fixed pancaking angle θ_p, the bottom panel shows the measurements that take into account expansion (increasing poloidal height R_p).
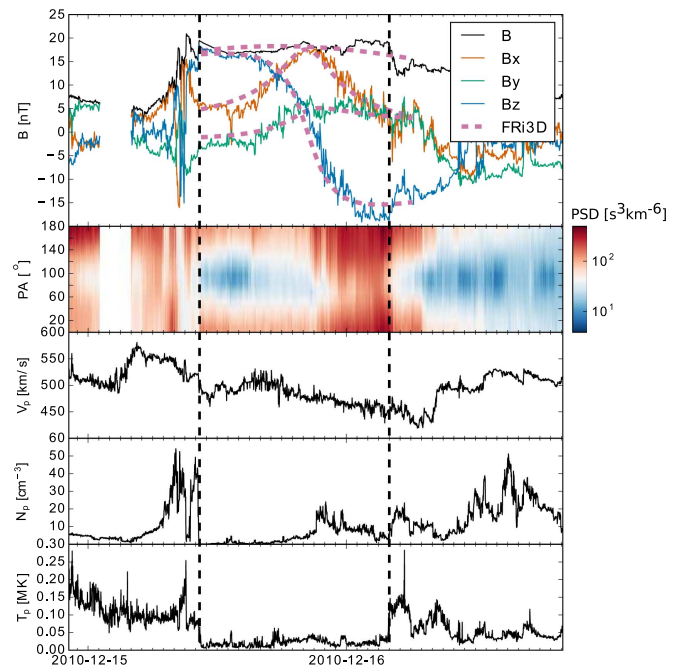

Figure 8. In-situ magnetic field and plasma measurements of the ICME launched on 2010 December 12 obtained by the *STEREO-A* spacecraft. The panels from top to bottom show magnetic field, electron pitch angle distribution, plasma bulk speed, proton density, and proton temperature. Magnetic field data are presented in HEEQ coordinates. Black vertical dashed lines show the time range of magnetic obstacle. Purple dashed curves show the FRi3D model fit.
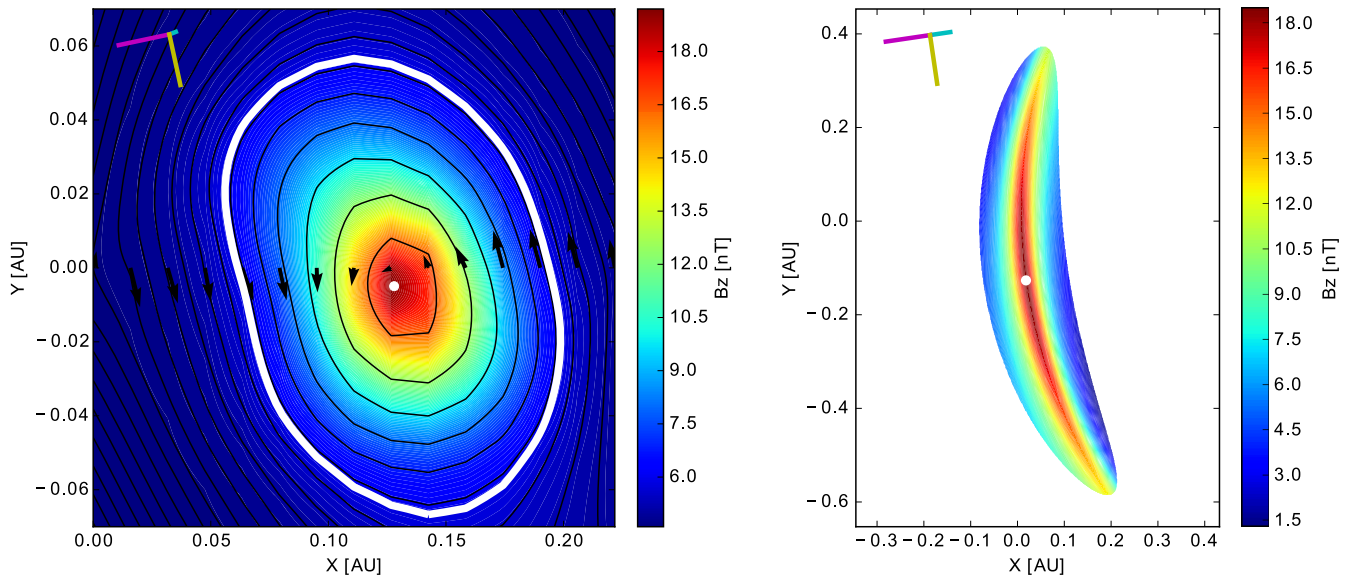
analyzed CME experienced overexpansion both in lateral and vertical directions, i.e., the increase of half-width φ_{hw} and pancaking angle θ_p (Patsourakos et al. 2010).

Figure 9. Magnetic field maps obtained using Grad–Shafranov reconstruction (left) and FRi3D fitting (right) for the CME released on 2010 December 12. Magnetic field component parallel to the local axis orientation of the CME is color-coded. The local CME axis is marked with the white dot. Projected trajectory of the spacecraft goes along the $Y = 0$ line. The Sun is to the right. In the top left corners of the maps, the projection of HEEQ coordinate system is shown as X_{HEEQ} (cyan), Y_{HEEQ} (magenta), and Z_{HEEQ} (yellow). White solid curve in GS magnetic field map marks the boundary of an unperturbed part of the flux rope. Black arrows show the projection of magnetic field measurements onto the cross-section plane.

We compare our modeling results with two of the most widely used conventional tools for CME research, i.e., GCS modeling of remote stereoscopic observations and Grad–Shafranov (GS) reconstruction of in-situ measurements. The results of GCS modeling (not shown in this study) are hard to visually distinguish from the ones of FRi3D modeling. Indeed, on early stages of CME evolution both pancaking and skewing deformations are not pronounced strong enough to demonstrate the discrepancies of the models in a clear way. Consequently, the differences in fitting parameters of the two models lie within the typical error boundaries of FM with the exception of the half-width φ_{hw}. The legs of a CME modeled by GCS represent two cones with radially oriented axes, while the legs of a FRi3D CME are curved according to Equation (14). Therefore, the half-width of a FRi3D fit is generally larger than the respective parameter of the GCS model even for visually similar fits.

Figure 9 shows how Grad–Shafranov reconstruction of the analyzed CME compares to corresponding cross-section of the FRi3D model. Note that the FRi3D model reproduces an evolving non-static CME and hence the right panel of Figure 9 shows only a snapshot of its cross-section. Distribution of B_Z component of magnetic field in the cross-section of the FRi3D model reveals slight asymmetry arising from the global 3D geometry of the structure. The orientation of the invariant axis obtained via GS reconstruction differs from the local axis orientation of the FRi3D model by 17°. The most obvious difference between the two magnetic field maps is their shape. GS reconstruction produced an almost circular cross-section, while the FRi3D fit resulted in a strongly distorted pancake shape. Another important difference is the estimated impact distance, i.e., the closest distance between the trajectory of the spacecraft and the axis of a CME. The FRi3D model fit produced the impact distance of 0.124 au, while GS reconstruction estimated this parameter as 0.005 au. By integrating the GS reconstructed magnetic field map using Equation (17), we estimate the magnetic flux to be 3.3×10^{12} Wb, which is

significantly lower than 4.7×10^{14} Wb predicted by the FRi3D model. There are multiple possible explanations for such a mismatch. On the one hand, since the shape of the flux-rope cross-section estimated by GS reconstruction does not take into account pancaking distortion, its area is likely to be underestimated, which in turn could lead to the underestimation of the total magnetic flux. On the other hand, given that the typical flux budget of an active region is of the order of 10^{14} Wb, the FRi3D model seems to overestimate the magnetic flux released with a CME. This issue in turn could result from the underestimation of field line twist near the edge of the structure and the usage of magnetic field distribution in the flux-rope cross-section described by Equation (16).

In the second case study, we investigate a CME that was released on 2011 October 1 at 21:00 UT from the northern hemisphere. This eruption is associated with a B9 class flare observed at −117° longitude and 19° latitude in Stonyhurst coordinates (Thompson 2006). The event was observed by coronagraphs on board *SOHO* and *STEREO* (see Figure 10). It produced a full halo in the *STEREO-B* field of view and a backside full halo in the *STEREO-A* field of view. This fast CME propagated through the coronagraph field of view with a projected speed of 1238 km s^{-1} and produced a clear shock wave front.

Lower panels of Figure 10 show the fitting of the FRi3D model to coronagraph images from COR2 and C3 instruments. Again, the model well describes the observations in a similar fashion as GCS. Key geometrical parameters of the model fit are listed in Table 2.

The interplanetary counterpart of this CME reached the *STEREO-B* spacecraft on 2011 October 3. The shock wave produced by the fast ejecta was registered on 2011 October 3 at 22:23 UT, while the magnetic obstacle was measured between 02:00 UT and 12:40 UT of 2011 October 4 (see Figure 11).

We carry the numerical fitting of the FRi3D model to in-situ data for this event using the same procedure as for the previous one with one exception. The rapid decrease of the total
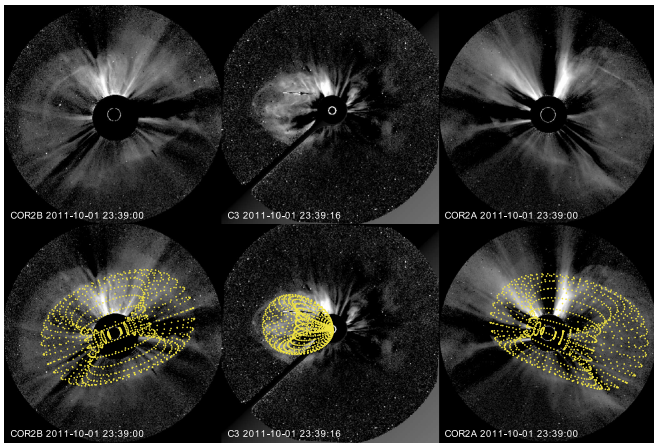
Figure 10. Coronagraph images of the CME released on 2011 October 1. The images from left to right show observations from COR2 coronagraph of *STEREO-B*, C3 coronagraph of *SOHO*, and COR2 coronagraph of *STEREO-B* respectively. Lower panels show the fitting of the FRi3D model to coronagraph observations.

Table 2
Parameters of the FRi3D Model Fits to Remote and in-situ Data for CME Launched on 2011 October 1

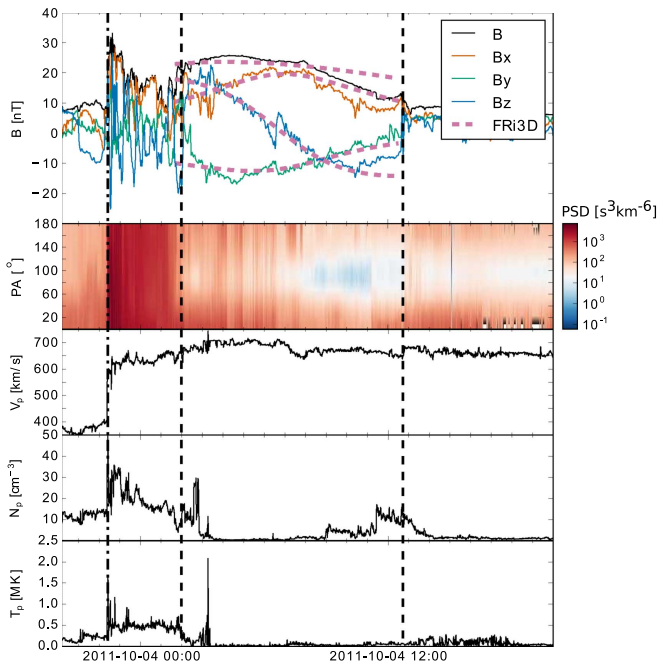|	θ	φ	$\langle R_p \rangle / R_t$	φ_{hw}	γ	n	θ_p
Remote	5.5	−95.0	0.30	75.0	21.0	0.55	27.0
in-situ	−0.3	−73.6	0.08	79.5	8.5	0.71	36.2
⋯			$\tau = 1.2$, $\Phi = 6.8 \times 10^{14}$ Wb, $V_{R_p} = 36.7$ km s^{-1}				
⋯			east–west polarity, left-handed				

Figure 11. In-situ magnetic field and plasma measurements of the ICME launched on 2011 October 1 obtained by the *STEREO-B* spacecraft. The panels from top to bottom show magnetic field, electron pitch angle distribution, plasma bulk speed, proton density, and proton temperature. Magnetic field data are presented in HEEQ coordinates. Black vertical dashed lines show the time range of magnetic obstacle. Purple dashed curves show the FRi3D model fit.

magnetic field in the rear part of the magnetic obstacle may be treated as a signature of flux-rope expansion. Thus we take expansion into account by plugging linearly growing poloidal height R_p defined by Equation (21) into the model.

The results of the fit are shown in Figure 11 and the fitting parameters are listed in Table 2. The average euclidean distance between the modeled and real data is 3.53 nT.

According to our fits the CME deflected and rotated toward the solar equatorial plane and overexpanded in lateral and vertical directions. The estimated speed of poloidal expansion of the structure is $V_{R_p} = 36.7$ km s^{-1}, which seems to be a reasonable rate according to in-situ measurements. The modeled CME has a particularly low twist of 1.2 full rotations of magnetic field lines from footpoint to footpoint, which, however, is in good agreement with results reported by Hu et al. (2015). Our analysis showed that the CME experienced longitudinal deflection by 21°.4 eastward. However, a fast CME is expected to experience westward longitudinal deflection due to interaction with the background magnetic field, which expands radially with slower solar wind and forms the Parker spiral (Wang et al. 2004; Isavnin et al. 2013). Such a result has multiple possible explanations. First, error bars of the FRi3D model fits are not well-known yet. Extensive statistical studies and comparison with MHD simulations, which are the subjects for follow-up research, would quantify the uncertainties of the fits. Second, estimated longitudinal deflection could be a result of non-radial expansion of the CME. The difference between longitudinal location of the source region (−117°) and direction of propagation estimated from remote observations (−95°) shows that the CME is likely to have experienced eastward deflection by 22° in the lower corona. One could speculate that eastward drift of the structure slowly continued in the inner heliosphere. Third, interaction with the Parker spiral is more pronounced for weak magnetic field CMEs, while the analyzed event exhibits relatively strong magnetic flux (Kay et al. 2015).

Figure 12 shows side by side magnetic field maps calculated using the GS reconstruction technique and FRi3D fitting respectively. The orientation of the invariant axis obtained via GS reconstruction differs from the local axis orientation of the FRi3D model by 40°. According to the FRi3D fitting, the CME experienced strong expansion, while GS reconstruction again resulted in an almost circular shaped cross-section. The impact distance according to the FRi3D model is 0.106 au, which significantly exceeds the 0.017 au estimate by GS reconstruction. By integrating the GS reconstructed magnetic field map using Equation (17), we estimate the magnetic flux to be 2.7×10^{12} Wb, again showing mismatch with 6.8×10^{14} Wb predicted by the FRi3D model. Possible reasons for this discrepancy are the same as we outlined earlier.

4. DISCUSSION AND OUTLOOK

We presented the first 3D model that is able to describe consistently both remote and in-situ observations of CMEs. The FRi3D model encapsulates both global geometry and 3D magnetic structure of a CME and is able to reproduce its morphological and geometrical structure with a high degree of complexity. We applied the model for analysis of two example CMEs. Independent model fits to remote and in-situ measurements of analyzed CMEs were found to provide a consistent
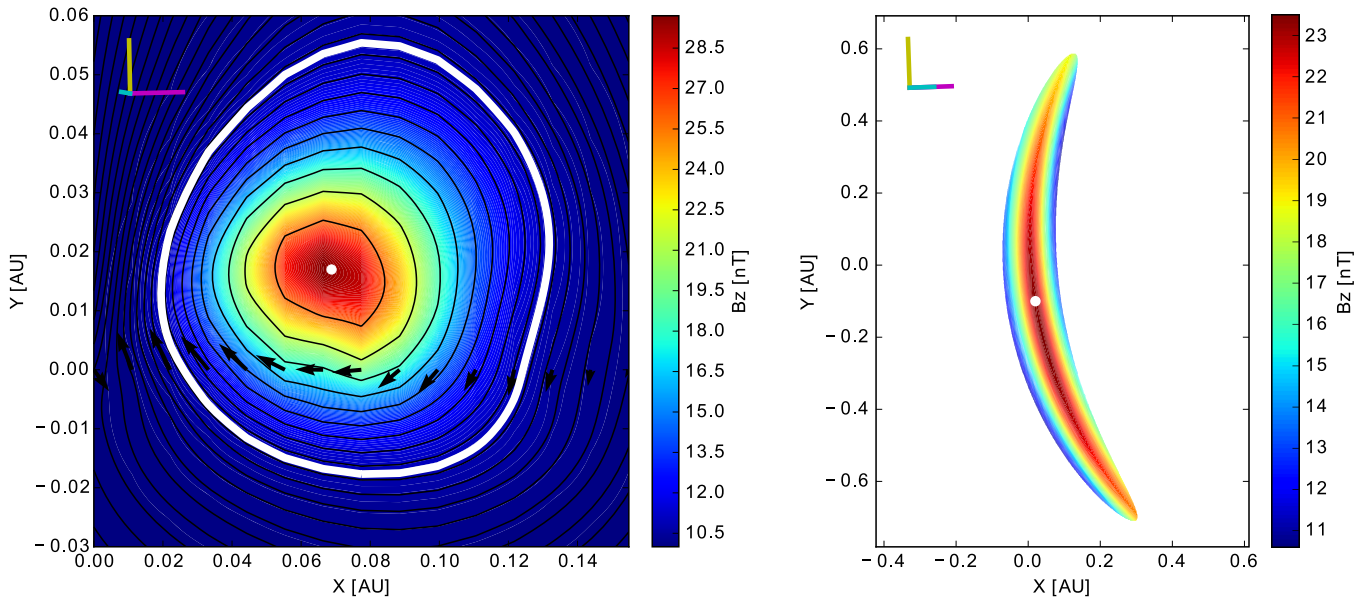
Figure 12. Magnetic field maps obtained using Grad–Shafranov reconstruction (left) and FRi3D fitting (right) for the CME released on 2011 October 1. The magnetic field component parallel to the local axis orientation of the CME is color-coded. The local CME axis is marked with the white dot. Projected trajectory of the spacecraft goes along the $Y = 0$ line. The Sun is to the right. In the top left corners of the maps, the projection of the HEEQ coordinate system is shown as X_{HEEQ} (cyan), Y_{HEEQ} (magenta), and Z_{HEEQ} (yellow). The white solid curve in the GS magnetic field map marks the boundary of an unperturbed part of the flux rope. Black arrows show the projection of magnetic field measurements onto the cross-section plane.

description of their global configuration. The deduced properties of CME evolution were found to support earlier research on this subject, e.g., CMEs were found to deflect and rotate toward the solar equatorial plane.

The FRi3D model uses a relatively large amount of free parameters compared to traditional flux-rope fitting and reconstruction techniques, which can lead to concerns about uniqueness of model fits. However, after applying the model for analysis of two example CMEs, we did not find that it is the case. One possible reason could be the connection of the model to the Sun. This geometrical feature poses a strong constraint on model parameters and is exempt from the majority of traditional local flux-rope fitting techniques. Another plausible explanation is the clarity of events selected for case studies, i.e., ambiguities could rise for more distorted CMEs.

A 3D configuration of magnetic field with constant twist is constructed on the basis of empirical findings and thus it is not guaranteed or checked that the FRi3D model is force-free. Multiple studies indicated that magnetic clouds associated with CMEs tend to have pressure gradients that cannot be explained with a force-free approximation (Mulligan & Russel 2001; Hidalgo et al. 2002a; Möstl et al. 2009a). A possible contribution to these features could be the global geometry of CMEs, which is far from cylindrical. Consequently, we do not treat the lack of force-free approximation as a disadvantage of the model.

Comparison with GS reconstruction showed that the FRi3D model does not seem to suffer from the typical shortcomings of conventional flux-rope fitting and reconstruction techniques, i.e., non-realistic shape of the cross-section and underestimation of impact distance (Riley et al. 2004). Nevertheless, distribution of the magnetic field from the edge to the center of the flux-rope cross-section, i.e., its minimum and maximum values, was found to be consistent with GS technique results.

The FRi3D model seems to overestimate the magnetic flux budget of a CME. This effect might result from the

underestimation of magnetic field line twist near the edge of a flux rope as well as inability of the Lundquist model (Equation (16)) to properly describe the distribution of magnetic field in pancaked cross-sections. In our further studies, we will tackle this issue with at least the following approaches. First, we will test the version of the model with the constant-twist rate, i.e., the amount of twist per unit length of a field line. Second, we will check the possibility to plug in the Gold and Hoyle constant-twist nonlinear force-free model (Gold & Hoyle 1960) into the FRi3D.

3D modeling of CMEs is a relatively new area of space weather research and hence there are a lot of possible fitting strategies that can be applied to a model like FRi3D. In fact, for testing purposes, in our example CME studies, we selected the worst case scenario, i.e., we fitted the model to remote and in-situ observations completely independently. Such a strategy is good for the demonstration of consistency of the model fits. However, the full potential of 3D modeling is unleashed by fitting an evolving model to a series of CME observations. In this scenario, a subset of free parameters of the model is assigned with evolution profiles expressed by any functions, e.g., linear evolution profiles represented by Equations (20) and (21). The evolving model is then fitted to all available data, i.e., coronagraph images, heliospheric imager observations, and in-situ measurements at any heliocentric distance. Thereafter, the fitted model can be used to predict further CME evolution. Such an approach could be the first step to the development of innovative space weather forecasting tools that would address the prediction of both the arrival time of a CME and the magnetic field produced by it at a given point of interplanetary space.

REFERENCES

Cargill, P. J. 2004, SoPh, 221, 135
Chen, P. F. 2011, LRSP, 8, 1
Daglis, I. A. 2001, in NATO Science Ser. 38, Space Storms and Space Weather Hazards (Netherlands: Springer)
Davies, J. A., Perry, C. H., Trines, R. M. G. M., et al. 2013, ApJ, 777, 167
Démoulin, P., Janvier, M., Masías-Meza, J. J., & Dasso, S. 2016, A&A, 595, A19
Domingo, V., Fleck, B., & Poland, A. I. 1995, SoPh, 162, 1
Eyles, C. J., Harrison, R. A., Davis, C. J., et al. 2009, SoPh, 254, 387
Gold, T., & Hoyle, F. 1960, MNRAS, 120, 89
Gui, B., Shen, C., Wang, Y., et al. 2011, SoPh, 271, 111
Hidalgo, M. A., Cid, C., Viñas, A. F., & Sequeiros, J. 2002a, JGR, 107, SSH1
Hidalgo, M. A., Nieves-Chinchilla, T., & Cid, C. 2002b, GeoRL, 29, 1637
Hu, Q., Qiu, J., & Krucker, S. 2015, JGRA, 120, 5266
Hu, Q., & Sonnerup, B. U. Ö. 2002, JGR, 107, 1142
Isavnin, A., Kilpua, E. K. J., & Koskinen, H. E. J. 2011, SoPh, 273, 205
Isavnin, A., Vourlidas, A., & Kilpua, E. K. J. 2013, SoPh, 284, 203
Isavnin, A., Vourlidas, A., & Kilpua, E. K. J. 2014, SoPh, 289, 2141
Janvier, M., Démoulin, P., & Dasso, S. 2013, A&A, 556, A50
Kaiser, M. L., Kucera, T. A., Davila, J. M., et al. 2008, SSRv, 136, 5
Kay, C., Opher, M., & Evans, R. M. 2013, ApJ, 775, 5
Kay, C., Opher, M., & Evans, R. M. 2015, ApJ, 805, 168
Kilpua, E. K. J., Isavnin, A., Vourlidas, A., Koskinen, H. E. J., & Rodriguez, L. 2013, AnGeo, 31, 1251
Lanzerotti, L. J. 2011, in Space Storms and Space Weather Hazards, ed. I. A. Daglis (Dordrecht: Kluwer), 313

Lee, J.-O., Moon, Y.-J., Lee, K.-S., & Kim, R.-S. 2014, SoPh, 289, 2233
Lugaz, N., Vourlidas, A., & Roussev, I. I. 2009, AnGeo, 27, 3479
Lundquist, S. 1950, Ark. Fys., 2, 361
Möstl, C., & Davies, J. A. 2013, SoPh, 285, 411
Möstl, C., Farrugia, C. J., Biernat, H. K., et al. 2009a, AnGeo, 27, 2215
Möstl, C., Farrugia, C. J., Biernat, H. K., et al. 2009b, SoPh, 256, 427
Mulligan, T., & Russel, C. T. 2001, JGR, 106, 10581
Nieves-Chinchilla, T., Linton, M. G., Hidalgo, M. A., et al. 2016, ApJ, 823, 27
Owens, M. J., Merkin, V. G., & Riley, P. 2006, JGR, 111, A3
Patsourakos, S., Vourlidas, A., & Stenborg, G. 2010, ApJL, 724, L188
Patsourakos, S., Vourlidas, A., & Stenborg, G. 2013, ApJ, 764, 125
Poomvises, W., Zhang, J., & Olmedo, O. 2010, ApJL, 717, L159
Riley, P., Linker, J., Lionello, R., et al. 2004, JASTP, 66, 1321
Rollett, T., Temmer, M., Möstl, C., et al. 2013, SoPh, 283, 541
Russell, C. T. 1999, AuJPh, 52, 733
Storn, R., & Price, K. 1997, J. of Glob. Opt., 11, 341
Thernisien, A., Vourlidas, A., & Howard, R. A. 2009, SoPh, 256, 111
Thernisien, A. F. R., Howard, R. A., & Vourlidas, A. 2006, ApJ, 652, 763
Thompson, W. T. 2006, A&A, 449, 791
Vakil, A., & Green, S. I. 2009, CF, 38, 1771
Vourlidas, A. 2014, PPCF, 56, 064001
Vourlidas, A., Colaninno, R., Noeves-Chinchilla, T., & Stenborg, G. 2011, ApJL, 733, L23
Vršnak, B., Žic, T., Vrbanec, D., et al. 2013, SoPh, 285, 295
Wang, Y., Shen, C., Wang, S., & Ye, P. 2004, SoPh, 222, 329
Yurchyshyn, V., Abramenko, V., & Tripathi, D. 2009, ApJ, 705, 426
Zurbuchen, T. H., & Richardson, I. G. 2006, SSRv, 123, 31